Cerebral Cortex, April 2020;30: 2615–2626

doi: 10.1093/cercor/bhz264
Advance Access Publication Date: 28 January 2020
Original Article

ORIGINAL ARTICLE

Subthalamic Nucleus Activity Influences Sensory and Motor Cortex during Force Transduction

Ahmad Alhourani[1], Anna Korzeniewska[2], Thomas A. Wozny[3], Witold J. Lipski[3], Efstathios D. Kondylis[3], Avniel S. Ghuman[3,4], Nathan E. Crone[2], Donald J. Crammond[3], Robert S. Turner[4,5] and R. Mark Richardson[6,7]

[1]Department of Neurological Surgery, University of Louisville, Louisville, KY 40292, USA, [2]Department of Neurology, Johns Hopkins University School of Medicine, Baltimore, MD 21287, USA, [3]Department of Neurological Surgery, University of Pittsburgh, Pittsburgh, PA 15213, USA, [4]Brain Institute, University of Pittsburgh, Pittsburgh, PA 15260, USA, [5]Department of Neurobiology, University of Pittsburgh School of Medicine, Pittsburgh, PA 15213, USA, [6]Department of Neurosurgery, Massachusetts General Hospital, Boston, MA 02114, USA, and [7]Harvard Medical School, Boston, MA 02115, USA

Address correspondence to Mark Richardson, Department of Neurosurgery, Massachusetts General Hospital, 55 Fruit St., Gray 502, Boston, MA 02114, USA; E-mail: mark.richardson@mgh.harvard.edu.

Abstract

The subthalamic nucleus (STN) is proposed to participate in pausing, or alternately, in dynamic scaling of behavioral responses, roles that have conflicting implications for understanding STN function in the context of deep brain stimulation (DBS) therapy. To examine the nature of event-related STN activity and subthalamic-cortical dynamics, we performed primary motor and somatosensory electrocorticography while subjects ($n = 10$) performed a grip force task during DBS implantation surgery. Phase-locking analyses demonstrated periods of STN-cortical coherence that bracketed force transduction, in both beta and gamma ranges. Event-related causality measures demonstrated that both STN beta and gamma activity predicted motor cortical beta and gamma activity not only during force generation but also prior to movement onset. These findings are consistent with the idea that the STN participates in motor planning, in addition to the modulation of ongoing movement. We also demonstrated bidirectional information flow between the STN and somatosensory cortex in both beta and gamma range frequencies, suggesting robust STN participation in somatosensory integration. In fact, interactions in beta activity between the STN and somatosensory cortex, and not between STN and motor cortex, predicted PD symptom severity. Thus, the STN contributes to multiple aspects of sensorimotor behavior dynamically across time.

Key words: deep brain stimulation, electrocorticography, sensory integration, subthalamic nucleus

Introduction

Understanding the network-level encoding of movement is critical for improving basal ganglia-thalamocortical circuit models, for developing closed-loop deep brain stimulation (DBS) paradigms, and for developing brain–computer interfaces that combine cortical and subcortical signals to control neuroprosthetic devices. Movement-related information transfer in the cortex is thought to be reflected in the coupling of local field potentials (LFPs), where event-related broadband gamma activity indexes population firing of local principal neurons (Manning et al. 2009). Slower oscillations, such as those in the beta frequency band (13–30 Hz), represent

rhythmic fluctuations of neuronal excitability that may serve to coordinate information transfer between regions (Jensen et al. 2005; Yamawaki et al. 2008), including within the basal ganglia-thalamocortical network (Kondylis et al. 2016; Lipski et al. 2017). How specific cortical–subcortical interactions encode specific aspects of movement is not well understood. Invasive recordings in subjects implanted with DBS electrodes in the basal ganglia represent the optimal paradigm for obtaining this information from humans, for instance demonstrating that subthalamic nucleus (STN) gamma oscillations may reflect necessary processing for motor state changes (Fischer et al. 2017), and that STN spike-to-cortical gamma phase coupling may have a role in neuronal communication prior to movement initiation (Fischer et al. 2018).

The STN is a primary DBS target used in the treatment of Parkinson's disease (PD) that receives cortical input directly from the frontal lobe and indirectly through the striatum, as demonstrated in rodent (Afsharpour 1985; Nambu et al. 1997) and nonhuman primate (NHP) tracing studies (Haynes and Haber 2013). Studies examining LFP recorded from the STN with simultaneous recordings from scalp EEG or MEG demonstrated that gamma and beta frequency band activities are coherent between cortical sources and the STN (Fogelson et al. 2006; Litvak et al. 2012), a relationship modulated by medication (Williams 2002) and movement (Lalo et al. 2008; Litvak et al. 2012), and confirmed by electrocorticography (Swann et al. 2016). Recordings using EEG (Lalo et al. 2008) and MEG (Litvak et al. 2012) have suggested that cortical beta band activity drives activity in the STN at rest, a casual interaction that is attenuated with movement (Litvak et al. 2012). EEG and MEG recordings, however, do not have sufficient spatial resolution for reliably localizing the specific anatomical source of cortical oscillations at the level required for precise causal analyses, to differentiate activity originating in primary motor (M1) from that in primary sensory (S1) cortex. Due to low signal-to-noise ratios (SNRs), these methods also have proven insufficient for identifying gamma-range causal interactions during movement (Lalo et al. 2008; Litvak et al. 2012).

The recent adaptation of electrocorticography for intraoperative neurophysiology research in subjects undergoing DBS safely allows for the recording of cortical LFP activity during the awake portion of the procedure, while patients perform behavioral tasks (Panov et al. 2017). To define the dynamics of movement-related information transfer between the cortex and STN, we employed intracranial recording techniques (Crowell et al. 2012) to collect simultaneous LFP recordings from primary motor cortex (M1), primary somatosensory cortex (S1), and the STN, during a hand grip task (Kondylis et al. 2016). In addition to classical measures of movement-related spectral dynamics, including power and phase coherence, we used event-related causality (ERC) analysis, a multivariate autoregressive (MVAR) technique that estimates causality in multichannel data (Korzeniewska et al. 2008), to define the temporal evolution of task-related causal influences in both beta and gamma frequency ranges and to determine whether these influences are associated with Parkinsonian motor symptoms.

Methods

Subjects

Study subjects underwent bilateral STN DBS lead implantation, as recommended by a multidisciplinary review board based on standard clinical indications and inclusion/exclusion criteria. Subject demographics are shown in Table 1. Informed consent for the placement of the research ECoG strip electrode was obtained prior to surgery, in accordance with a protocol approved by the Institutional Review Board of the University of Pittsburgh (IRB Protocol #PRO13110420). UPDRS Part III scores were collected by neurologists specializing in movement disorders, collected during scheduled clinic visits 1–3 months prior to surgery. UPDRS scores are reported for the off-medication condition.

Behavioral Paradigm

The subjects performed a visually cued, instructed delay handgrip task with monetary reward, as previously described (Kondylis et al. 2016a). The task was performed intra-operatively after the implantation of the DBS lead, approximately 1 hour after cessation of anesthesia sedation. Briefly, a trial began with simultaneous presentation of a yellow traffic light in the center of the screen, and a cue on one side indicating which hand the patient should use for the subsequent response (squeezing the handgrip). The cue remained on the screen for 1000–2000 ms, following which the traffic light changed to either green (Go cue) or red (No-Go cue). A grip force response $\geq$10% of a previously measured maximum voluntary grip force for $\geq$100 ms, within 2 s of the Go cue onset on the correct side was considered a successful Go trial. A trial was counted as an error if subjects either did not meet these criteria or inappropriately squeezed during a No-Go trial. Finally, a feedback message cued the subject to stop squeezing the handgrip and indicated the dollar amount won or lost for the trial, as well as a running balance of winnings. Each trial was followed by a variable intertrial interval of 500–1000 ms. A desire to reduce overall intra-operative task time precluded using a longer intertrial interval that would have completely precluded potential interactions from previous trials. Subjects performed the task for a cumulative total of 10 to 25 min, and only data from subjects who achieved >20 successful trials for each hand were analyzed. The trial design included a higher ratio of Go to No-Go trials and time constraints in the operating room lead to the number of overall No-Go trials being too low to analyze any effects for effects.

Electrophysiological Recordings

ECoG data were recorded intra-operatively from subjects with movement disorders using a standard four-contact ($n=1$), six-contact ($n=5$), or eight-contact ($n=3$) strip electrode (2.3-mm exposed electrode diameter, 10-mm inter electrode distance) (Ad-Tech, Medical Instrument Corporation), temporarily implanted through the burr hole used for DBS lead implantation as previously described (Crowell et al. 2012; Kondylis et al. 2016a). In one subject, a 2×14-contact electrode was used (1.2-mm exposed electrode diameter, 4-mm inter electrode distance). LFPs from the STN were recorded using the clinical DBS lead (model 3389, Medtronic) from all four contacts and referenced offline in a bipolar montage (except for one subject, in which the STN LFPs were recorded from a ring contact located 3 mm superior to the tip of the three microelectrodes used for microelectrode recordings), sampled at 1375 Hz, and referenced offline in a common average montage. A referential montage was used with the reference electrode placed in the scalp and a ground electrode placed in the skin overlying the acromion process. Antiparkinsonian medications were held for at least 12 hours prior to

Table 1 Subject characteristics

Subject	Age (Gender)	Disease duration (years)	MMSE	Rest tremor		Action tremor		Finger taps		Hand grip		RAM	
				R	L	R	L	R	L	R	L	R	L
P1	44 (M)	10+	29/30	3/3	3/3	4/3	4/3	0/0	1/1	0/0	1/1	0/0	1/1
P2	52 (M)	12	27/30	1/0	3/0	1/0	1/0	2/0	3/1	2/0	3/1	n.a.	n.a.
P3	59 (F)	7	29/30	2/0	3/0	1/0	1/0	2/1	3/2	2/1	2/1	2/1	2/1
P4	54 (M)	28	n.a.	n.a.	n.a.	n.a.	n.a.	n.a.	n.a.	n.a.	n.a.	n.a.	n.a.
P5	60 (M)	12	30/30	2/0	2/0	1/1	2/2	1/0.5	1/0.5	1/1	1/1	1/1	1/1
P6	46 (M)	4	29/30	0/0	1/0	0/0	1/0	2/1	3/1	2/1	3/2	n.a.	n.a.
P7	53 (M)	10	30/30	1/0	0/0	0/0	0/0	2/1	2/1	2/1	2/2	3/1	3/2
P8	66 (M)	10+	30/30	3/1	3/3	2/1	3/2	3/2	3/3	3/1	3/2	3/2	2/2
P9	51 (M)	10+	n.a.	0/0	0/0	0/1	0/0	1/0	1/1	1/0	1/0	1/0	1/0
P10	71 (M)	22	30/30	2/1	0/0	0/0	0/0	3/2	2/1	3/2	3/1	3/2	3/1

Note. Subject demographics. MMSE = mini-mental status exam, L = left, R = right, RAM = rapid alternating movements, n.a. = not available in the medical record.

intra-operative testing. LFP data from the lead were obtained after clinical stimulation testing was completed. Subjects were fully awake, without the administration of anesthetic agents for at least 1 hour prior to task performance. No medication was given during task performance. Seven subjects underwent unilateral recordings from the left side during task performance, and three subjects performed the task on both sides. ECoG and STN signals were filtered (0.3–7.5 kHz), amplified, and digitized at 30 kHz using a Grapevine neural interface processor (Ripple Inc.).

The task paradigm was implemented using Psychophysics Toolbox (Brainard 1997) on a portable computer. Force signals from the handgrips and triggers marking the presentation of visual cues were digitally recorded simultaneously with the ECoG signals. Movement onset was calculated offline by smoothing force signals (15-ms running average) and using a 50-N/s threshold to detect changes in the rate of force generation. The onset of derived grip force data was used to segment ECoG data, and the triggers were used to isolate successful, contralateral Go trials.

Electrode Localization

Subdural electrode strips were implanted temporarily through standard frontal burr holes located near the coronal suture and aimed posteriorly to the hand knob, which had been stereotacticly identified with overlying scalp location marked as previously described (Kondylis et al. 2016). Subdural electrodes were localized using a custom method to align pre-operative MRI, intra-operative fluoroscopy, and postoperative CT; representative images of this technique were detailed previously (Randazzo et al. 2016). Briefly, the CT and MRI were co-registered using mutual information in the SPM software package and rendered into 3D skull and brain surfaces using Osirix (v7.5) (Rosset et al. 2004) and Freesurfer (v5.3) softwares (Dale et al. 1999), respectively. These surfaces and the fluoroscopy image were then loaded into a custom MATLAB user interface and aligned using common landmarks: stereotactic frame pins, implanted depth electrodes, and skull outline. The parallax effect of the fluoroscopic images was accounted for using the measured distance from the radiation source to the subject's skull. Following surface-to-fluoroscopic image alignment, a 3D location for each electrode was projected from the fluoroscopic image onto the cortical surface. Based upon the cortical parcellation for each subject's anatomy (Desikan et al. 2006), each electrode was assigned to a cortical gyrus. Electrodes were then grouped into anatomical regions of interest (ROIs), and electrode locations for the entire cohort in relation to M1 and S1 are displayed in Supplementary Figure 1. DBS electrodes were localized from postoperative imaging using lead-DBS (Horn et al. 2019) and transformed into a standard template for group visualization. The active contacts across the cohort were then plotted on a template STN (Ewert et al. 2018) (Supplementary Fig. 2).

Data Preprocessing

All electrophysiological data were preprocessed in MATLAB using custom scripts. First, DC offsets were removed from each channel. Line noise at 60 Hz and its harmonics was removed using a notch filter (MATLAB function idealfilter). Next, the data were low-pass filtered at 400 Hz using zero-phase finite impulse response (FIR) filters custom designed in MATLAB. The data were resampled to a sampling frequency of 1200 Hz in two steps. Channels with extensive artifact from movement, powerline, or environmental sources were visually identified and removed from further analysis. To minimize noise and ensure recordings were comparable across acquisition environments, LFP signals were rereferenced offline to a bipolar montage for the STN channels and to common average reference for the cortical ECoG channels. All trial epochs were visually inspected for any residual artifact and trials with any contaminated segments were rejected.

Electrode Selection

Electrode contacts were selected for further analysis based on anatomical and functional considerations. First, only the cortical electrodes localized to M1 (precentral gyrus) and S1 (postcentral gyrus) were included. Event-related potentials (ERPs) centered on movement onset were then used as an independent physiologic measure to select electrode contacts for subsequent time–frequency analyses. Briefly, the mean voltage during baseline was subtracted from the ERP, and each time point was tested against zero using a *t*-test. Surrogate ERPs were constructed from randomly sampled time points and tested the same way. An electrode was considered functionally activated if it showed a cluster of time points with a *t*-statistic sum greater than the 95% of the cluster sums in the null distribution from the surrogate ERPs (Groppe et al. 2011).

Spectral Analysis

Event-Related Amplitude Modulation

Channel data were temporally convolved with complex Morlet wavelets to obtain the instantaneous spectral components of the signal (Tallon-Baudry et al. 1999). The wavelet transform was calculated in steps of 2 Hz from 10 to 34 Hz for the beta band and in steps of 5 Hz from 50 to 150 Hz for the gamma band. The modulus of the complex signal, representing the analytical amplitude for each band, was divided into 3.5-s epochs surrounding movement onset (1.5-s premovement and 2 s of postmovement).

Interregional Phase-Locking

Phase-locking value (PLV) measures interregional synchrony by quantifying the consistency in phase difference across trials relative to a stimulus (Lachaux et al. 1999). While both amplitude and phase covariance contribute to classical measures of coherence, PLV relies only on the phase information and is thus agnostic to power covariation which is advantageous when the network shows similar power changes across nodes. To compute PLV, channel data were temporally convolved with complex Morlet wavelets to obtain the instantaneous spectral components of the signal (Tallon-Baudry et al. 1999). The wavelet transform was calculated between 10 and 34 Hz in steps of 1 Hz for the beta band and between 60 and 115 Hz in steps of 2 Hz for the gamma band. The real and imaginary components of each time–frequency point were divided by the modulus of the vector to generate a signed, unit-length, complex-valued time series. Trial epochs were constructed as above. The PLV between two channels was calculated by taking the modulus of the mean of the complex-valued product of multiplying trial epochs from one channel with the complex conjugate of a second channel. The PLV for frequency band f between sources i and j was defined as:

$$PLV_f(j,k) = \left| \frac{1}{N} \sum_{n=1}^{N} e^{i(\varphi j - \varphi k j)} \right| (i,j) = \left| \frac{1}{N} \sum_{n=1}^{N} e^{i(\varphi i - \varphi j - \varphi k)} \right|,$$

where N is the number of trials and ϕ represents the phase of the data at the wavelet frequency f for sources j and k, resulting in a frequency-specific PLV, having a value from [0,1], where 0 represents total phase independence and 1 means that all phase values are equal between the two signals.

Event-Related Causality

PLV provides the bivariate representation of connectivity and thus it does not differentiate mutual contributions in networks with multiple nodes. To this end, we employed ERC which is based on the concept of Granger causality (Granger 1969) where for signal Y to be considered causally influenced by signal X, knowledge of X's past has to significantly improve the prediction of Y. ERC uses an MVAR model that enables the estimation of causality in multichannel data in short windows (Ding et al. 2000). It estimates only direct causal influences by using short-time direct Directed Transfer Function (SdDTF) and employs a semi-parametric regression model to investigate statistically significant event-related changes in effective connectivity across time (Korzeniewska et al. 2008, 2011). This family of methods has a specific advantage over other effective connectivity measures, in that it mitigates the effects of volume conduction by minimizing the effect of zero-phase-delay conduction, and it has been validated in previous ECoG work (Blinowska et al. 2010; Korzeniewska et al. 2011; Flinker et al. 2015; Nishida et al. 2017).

Briefly, for each subject, the signal was band-passed between 65 and 115 Hz, using an FIR filter as implemented in EEGLAB (Delorme and Makeig 2004). The signals were then downsampled to 400 Hz and segmented into 2048 sample (5.12 s) epochs centered on the response time. SdDTF was calculated in short windows of 0.3 s, shifted in time by 0.012 s, for multiple realizations of the same stochastic\ignorespacesprocess (many trials/repetitions of the task). Only channels meeting the channel selection criteria described above were included in the model. Multiple trials or task repetitions from the same subject may be treated as repeated realizations of the same stochastic process which is stationary over short periods. ERC values were statistically tested with a baseline distribution from a 1-s precue baseline and Bonferroni-corrected for multiple comparisons. ERC values passing significance were retained in the frequency range of 65–115 Hz, normalized within subject and averaged across subjects and anatomical regions. A similar procedure was applied for ERC analysis in the beta frequency band. However, the signal was band-pass filtered between 13 and 30 Hz and downsampled to 120 Hz. The window used for SdDTF calculation was 0.4-s long and shifted in time by 0.016 s. While ERC values for individual subjects represent statistically significant predictions, we tested whether the group showed consistent predictions at similar time periods. A right-sided t-test was used to test if the group ERC values at each time point were significantly above a mean of zero which represents a null hypothesis that there is no consistent ERC prediction at this time point. A false discovery rate of 5% was used to correct for multiple comparisons. Next, we sought to define time periods when ERC predictions in a certain direction were significantly larger. For each of the six flow directions, a pairwise comparison was performed between every two flows by performing a t-test at every time point whether the mean ERC values for a flow A was significantly different than the ERC values of flow B. A positive t-statistic means that flow A was larger, and a negative value means that flow B was larger. A cluster-based permutation procedure was performed to find the significant time periods by randomly assigning individual ERC value to each flow direction and performing the t-test as above 1000 times to construct a null distribution based on the maximal cluster t-statistic. A P-value was assigned to the clusters found in the real data based on their location relative to the null distribution.

Correlation with Disease Severity

Finally, we investigated the effect of disease severity on the measured spectral changes. For each subject, the average z-scored spectral measure at each location was correlated with their respective Unified Parkinson's Disease Rating Scale (UPDRS) Part III total score in the OFF-medication state at every time–frequency point (frequency–frequency point for PAC). The data from the two subjects with bilateral recordings were averaged prior to the correlation, and one patient was excluded due to the lack of a UPDRS score. To define significant correlations, the subject mapping of UPDRS scores was shuffled 1000 times to construct a surrogate distribution of correlation values. The real and surrogate correlations were z-scored to the mean and standard deviation of the surrogate distribution. Each z-score image was thresholded at a z-value corresponding to a P-value of 0.05. A P-value was assigned to the clusters of correlation in

the real data based on its percentile in the distribution of largest cluster z-score sum in the surrogates. We retained clusters with a corresponding *P*-value less than 0.05.

Statistical Analysis

Significance at the group level was assessed using paired cluster-based permutation testing (Maris and Oostenveld 2007). For spectral amplitude and PLV, we used a standard resampling technique to construct a surrogate baseline (Voytek et al. 2010). For spectral amplitude, surrogate trials were constructed by using randomly generated movement onset times to epoch trials as above. Surrogate PLVs were created by shuffling the trials in one channel, thus eliminating the trial dependence between the two channels (Lachaux et al. 1999). This procedure was repeated 1000 times and mean of surrogates was used as the baseline epoch for that channel. Measures from all the channels within an ROI were averaged on a per subject basis prior to group level statistics.

Briefly, a paired *t*-test was performed at every time–frequency point for both trial amplitude or phase-locking between the real group data and the group surrogate baseline for a given subject. The resulting *t*-statistics map was thresholded at a pixel *P*-value of 0.05. The sum of the *t*-statistics within the resulting clusters was calculated. The trial and baseline data were shuffled while retaining the subject mapping between trial and baseline and tested again as described for the real data. This procedure was repeated 1000 times to construct a null distribution based on the maximal cluster *t*-statistic found at each permutation. A *P*-value was assigned to the clusters found in the real data based on their location relative to the null distribution. To account for multiple comparisons concerning the number of ROIs and frequency bands, we applied a Holm–Bonferroni correction (Holm 1979) and only presented data for significant clusters after correction. Event timings for significant changes were based on the temporal bounds of the significant clusters.

A similar procedure was used for the ERC pairwise comparisons where a pooled-variance *t*-test was performed at each time point between the flows in each group and clustering was performed as above. A surrogate distribution was constructed from the combined flows and the new surrogate flows were tested similarly 1000 times to construct a null distribution based on the maximal cluster *t*-statistic. A *P*-value was assigned to each correlation cluster in the real data based on its percentile in the surrogate distribution constructed from the largest cluster z-scores in the surrogate correlations. We retained clusters with a corresponding *P*-value less than 0.05, after correction with an FDR value of 5%.

Results

Motor Performance

Ten subjects with PD were studied, three of whom performed the task during recording in both hemispheres, resulting in 13 total hemispheric recordings. The subjects' motor performance fell within the previously published performance range of a partially overlapping ($n = 3$) cohort of subjects performing the same task, whose measures of motor performance we previously reported to not differ from that of subjects with either essential tremor or no movement disorder (epilepsy subjects undergoing intracranial monitoring), in terms of reaction time (*t*-stat = 1.8, *P*-value = 0.08), time-to-peak (*t*-stat = 1.4, *P*-value = 0.18), and peak force (*t*-stat = 0.03, *P*-value = 0.97) (Kondylis et al. 2016a). The average movement duration, defined as the period from force inflection to return to baseline, was 1340 ± 238 ms (mean ± std). The evolution of force generation was stereotyped within subjects across trials, reaching peak force at an average of 630 ± 210 ms (mean ± std) in relation to movement onset, and returning to baseline on average at 1340 ± 238 ms (mean ± std).

ERPs coincident with the time of movement onset were calculated for all electrode recording channels and this independent measure of neural activation was used to select channels of interest for further analyses (Fig. 1). Twelve out of the thirteen ECoG recordings (9/10 subjects) showed a significant ERP response in both M1 and S1 gyri (1–3 contacts per region) with reversal of the ERP polarity indicating electrode locations on either side of the central sulcus in each case. In the remaining subject, no contacts were localized to S1, but a significant ERP response was found in contacts overlying M1. In the STN, at least one bipolar pair with a significant ERP response was found in 12 of 13 recordings, and the bipolar contact with the largest ERP for each subject was selected for further analysis. The one recording that lacked an ERP response in the STN was excluded from further analysis. Recordings appeared similar across hemispheres, but there were too few subjects to study interactions based on recording laterality or symptom asymmetry.

Event-Related Modulation of Oscillatory Activity

We found that movement was preceded by beta desynchronization across the motor circuit involving M1, S1, and the STN that was followed by an increase in gamma activity centered around movement as previously shown in the studies of the STN (Brown et al. 2001; Brittain et al. 2014) and the sensorimotor cortex (Crone 1998a, 1998b). Group-level analysis of spectral power changes during motor planning and execution demonstrated a common pattern of beta power modulation in each region. An early decrease in power began prior to movement onset and persisted throughout the movement epoch. This movement-related beta desynchronization appeared in close temporal fashion across locations, at −953 ms in M1 (cluster bounds: −953 to 805 ms/10–35 Hz, cluster *P*-value: <0.001), −937 ms in STN (cluster bounds: −937 to 952 ms/10–35 Hz, cluster *P*-value: <0.001), and −826 ms in S1 (cluster bounds: −826 to 979 ms/10–25 Hz, cluster *P*-value: <0.001). In all three regions, beta band power rebounded around the time of movement termination, at +1157 ms in STN (cluster bounds: +1157 to 2000 ms/12–35 Hz, cluster *P*-value: <0.01), +1384 ms in S1 (cluster bounds: +1384 to 2000 ms/10–35 Hz, cluster *P*-value: <0.02), and + 1479 ms in M1 (cluster bounds: +1479 to 2000 ms, cluster *P*-value: <0.04). Gamma modulation also occurred in each region, including S1. A circuit-wide increase in amplitude occurred in the immediate peri-movement period at −163 ms in M1 (cluster bounds: −163 to 552 ms/65–150 Hz, cluster *P*-value 0.0001), −105 ms in S1 (cluster bounds: −105 to 721 ms/60–150 Hz, cluster *P*-value 0.0012), and + 250 ms in STN (cluster bounds: +250 to 459 ms/60–100 Hz, cluster *P*-value 0.004). Changes in gamma activity spanned a broadband range in both cortical areas, while that in the STN occurred predominantly in a narrow band centered at 75 Hz (based on the weighted centroid of the cluster), as previously described for the basal ganglia (Jenkinson et al. 2013), with less modulation in broadband gamma (Fig. 2).

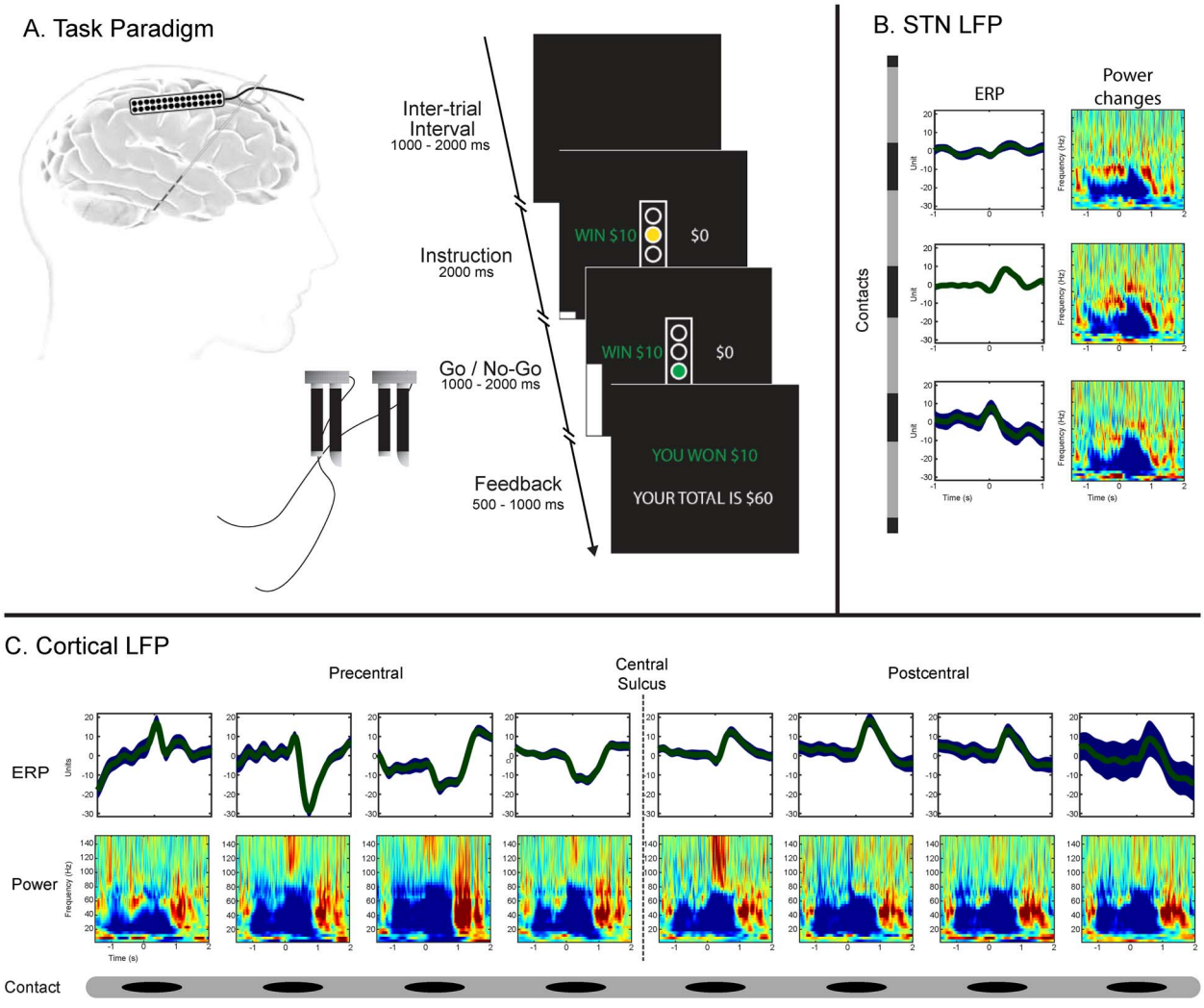

Figure 1. Schematic of experimental design. (*A*) A simplified schematic of the cue screens, intervals, and recording paradigm. Subjects squeezed grip-force transducers in response to visual stimuli. The intertrial interval duration was randomized on a per trial basis, while the Go/No-Go and feedback durations were adjusted per subject after a training session established how quickly the subject performed the task. Simultaneous recordings using (*C*) implanted subdural electrodes over motor and sensory cortices and (*B*) electrodes on the STN DBS lead demonstrate LFP changes in both locations. Movement was associated with an ERP in both the STN and cortical areas. The mean ERP (green) and standard deviation (blue) at each recoding contact are shown from a representative patient. Movement induced a similar pattern of spectral changes at all recording locations (power modulation shown as z-scores relative to a 1-s baseline at each recording site).

Interregional Phase-Locking

To begin to determine the importance of these changes in spectral power, we next examined whether concurrent movement-related amplitude and PAC changes were associated with interregional phase-locking between these three brain regions. With respect to beta activity, prior to movement, M1 exhibited epochs of significant beta phase-locking to both S1 (cluster bounds: −1500 to −1095 ms/10–35 Hz, cluster *P*-value: <0.001) and the STN (−1400 ms) (Fig. 2). Moreover, M1 beta phase-locking to the STN showed two patterns of synchronization: phase locking to low-beta (centered at 13 Hz) and a separate cluster of phase locking to high-beta (centered at 26 Hz). The low-beta cluster was sustained from −1400 to −450 ms (10–16 Hz, cluster *P*-value: <0.001), while the high-beta cluster consisted of two short periods of synchronization, from −1054 to −1191 ms and from −855 to −740 ms (16–33 Hz, cluster *P*-values: 0.02 and 0.001). A rebound phenomenon was observed across the entire network (M1 to S1: 870 to 2000 ms/10–35 Hz, cluster *P*-value: <0.01; STN to S1: +1052 to 1747 ms/11–28 Hz, cluster *P*-value: <0.01), with the M1 to STN beta phase-locking again exhibiting both a high beta cluster (1053 to 1191 ms/14–33 Hz, cluster *P*-value:<0.01) and a low-beta cluster (1576 to 2000 ms/10–27 Hz, cluster *P*-value: <0.001). Thus, STN-M1 phase locking at movement termination recapitulated the pattern seen prior to desynchronization.

Examining phase-locking in the gamma band, we found that phase-locking of STN to M1 and S1 bracketed movement onset and termination (Fig. 2). In the peri-movement period, brief phase-locking in the gamma band centered at 68 Hz was observed between M1 and the STN (cluster bounds: −45 to 38 ms/60–92 Hz, cluster *P*-value < 0.01) that was followed by M1-S1 phase-locking centered at 88 Hz (cluster bounds: 34 to 390 ms/60–115 Hz, cluster *P*-value < 0.01). Near movement termination, brief gamma phase-locking again was observed, between S1 and the STN centered at 92 Hz (cluster bounds:

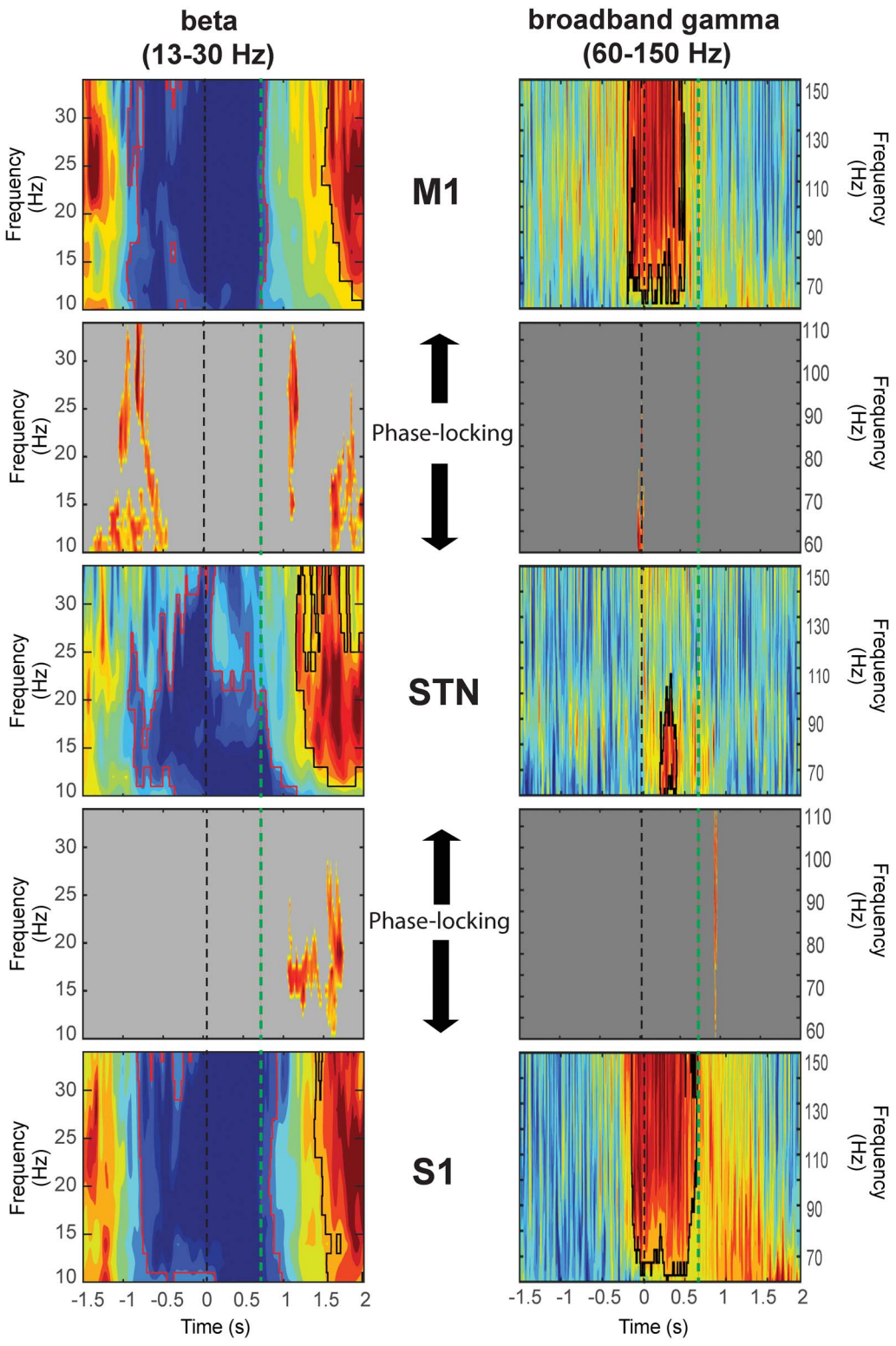

Figure 2. Regional power modulation and interregional functional coupling across the network. A cluster-based permutation test was used to define clusters of significant power changes (panels 1, 3, and 5) across subjects marked by a black border for significant increases and a red border for significant decreases. Significant functional coupling as measured by interregional phase-locking was defined in a similar fashion (panels 2 and 4) with only significant clusters being plotted. Black dotted line represents movement onset. Green dotted line represents time of peak force generation.

926 to 960 ms/62–115 Hz, cluster P-value < 0.01) and M1 to S1 centered at 89 Hz (cluster bounds: 1025 to 1496 ms/60–115 Hz, cluster P-value < 0.01). Although these gamma phase-locking results theoretically could result from an artifact of increased SNR in the gamma band, the epoch of movement-related gamma phase-locking preceded the epoch in which a significant gamma amplitude increase occurred. Similarly, phase-locking between S1 and M1 was similar in both epochs despite a difference in SNR. Thus, STN gamma phase is coordinated with that of M1 in relation to movement onset and is correlated with that in S1 in relation to movement termination.

Event-Related Causality

We next determined the propagation of neural activity between the STN, M1, and S1 during different movement periods, using ERC, which estimates the causal influences (in a statistical sense) between networked brain regions. We used ERC to estimate the direction, intensity, and temporal course of both beta and gamma activity propagation between these regions. We discovered bidirectional causal interactions in both beta and gamma bands across the temporal course of movement planning and execution, as might be expected. To better describe these interactions, we defined four time periods based on the average times our subjects moved: a motor planning period prior to movement, an early movement period from initiation (time zero) until reaching peak force, a late movement period from peak force until movement termination, and a termination period. Although ERC represents statistically significant changes in information flow compared with baseline, we additionally tested the results at the group level for significantly different pairwise ERC causal flows between regions, to determine whether the interaction dominated by flow from one region to the other was statistically significant in the group of patients.

For the beta band, significant bidirectional interactions occurred between all location pairs (Fig. 3). Prior to movement, STN influence on M1 (Fig. 3B—blue) and S1 (Fig. 3C—blue) predominated over cortical influences on the STN. In the case of communication between STN and S1, S1 influenced STN only briefly at a time near movement termination (Fig. 3C—green). In fact, the only region-pair demonstrating a statistically significant difference between pair-wise ERC magnitude was STN-S1, where STN beta strongly influenced S1 soon after movement onset (+132 to +292 ms, cluster P-value: <0.01) (Fig 3C—gray shadow).

Bidirectional gamma interactions between all region-pairs were more continuous than those for beta activity. M1 and S1 showed significantly increased bidirectional propagation throughout the entire trial epoch (indicated by the continuous colored lines at the top of Fig. 3D). The increase in the propagation of gamma activity from S1 to M1 peaked at +264 ms (Fig. 3D—green), while the increase in gamma propagation from M1 to S1 peaked at +672 ms (Fig. 3D—red), coinciding with peak force transduction. This later peak of predominant M1 to S1 propagation represented the only time of significant difference in ERC magnitudes in this region-pair (+612 to +732 ms, cluster P-value: <0.01) (Fig. 3D—gray shadow). M1 and STN also showed near-continuous significant increases in bidirectional gamma band causal interactions, with one epoch of predominant flow from STN to M1 beginning near the peak of force transduction (+672 to +1020 ms, cluster P-value: <0.01) (Fig. 3E—gray shadow). S1 and STN gamma band interactions were more variable (Fig. 3F), with significant bidirectional flow occurring throughout the trial epoch, but with no single periods demonstrating changes from baseline that were statistically predominant in one direction over the other.

Correlation with Parkinson's Severity

Finally, we assessed the relationship of each of the above directional measures to disease severity. Several ERC measures correlated with disease severity; however, only measures in the beta band were the only values found to be significantly correlated to the UPDRS Part III score in the OFF-medication state, after correction for multiple comparisons (Fig 4). Specifically, the strength of bidirectional interactions between STN and S1 during the motor planning epoch was negatively correlated with the UPDRS score. Stronger STN influence on S1 during movement termination also was negatively correlated with UPDRS scores.

Discussion

We employed intracranial recordings within the cortical-subthalamic network to determine the timing and causal nature of LFP interactions during force generation. The results provide the first evidence from humans that STN gamma activity can predict activity in the cortex not only during, but also prior to movement, consistent with the idea that the STN participates in both motor planning and execution. Additionally, we demonstrated that S1 plays a significant role in this process, as the STN exhibited distinct causal interactions with sensory cortex. We additionally discovered that STN beta causal interactions involving S1, but not M1, predicted disease severity, further indicating the importance of subcortical sensory integration during movement encoding.

Motor Planning and Execution

The STN has been proposed to have a role in motor planning, for instance in preventing or stopping an action, including inhibiting responses during the computation of a decision threshold (Herz et al. 2016; Fischer et al. 2017). For example, gamma power and decreases in STN-cortical synchrony have been correlated with successful stopping action (Fischer et al. 2017), and trial-wise variation in delta-theta oscillatory activity in the STN has been suggested to reflect decision thresholds (Herz et al. 2016). ERC revealed that STN activity prior to movement onset demonstrated information transfer in both gamma and beta bands despite the lack of power increase in both. In general, our findings align with the idea that STN gamma activity reflects dynamic processing that supports flexible motor control (Fischer et al. 2017).

Movement-related information transfer may occur through increased gamma synchrony that emerges as the neuronal populations are released from beta entrainment. Recent work supports a model in which cortical beta originates from bursts of synchronous synaptic drivers (Sherman et al. 2016), where the strength of this synchrony is reflected in the waveform properties of the LFP, and increased synchrony leads to nonsinusoidal beta waves, indexed by increased apparent PAC (Cole et al. 2017). Complementary evidence has also been reported in Parkinsonian NHPs, where prolonged STN beta bursts were observed as a marker for the emergence of PD-like symptoms (Deffains and Bergman 2019), and these parkinsonism-related β oscillations were found to resonate across the BG network through the STN. The exaggerated PAC seen in PD, therefore, may index over the

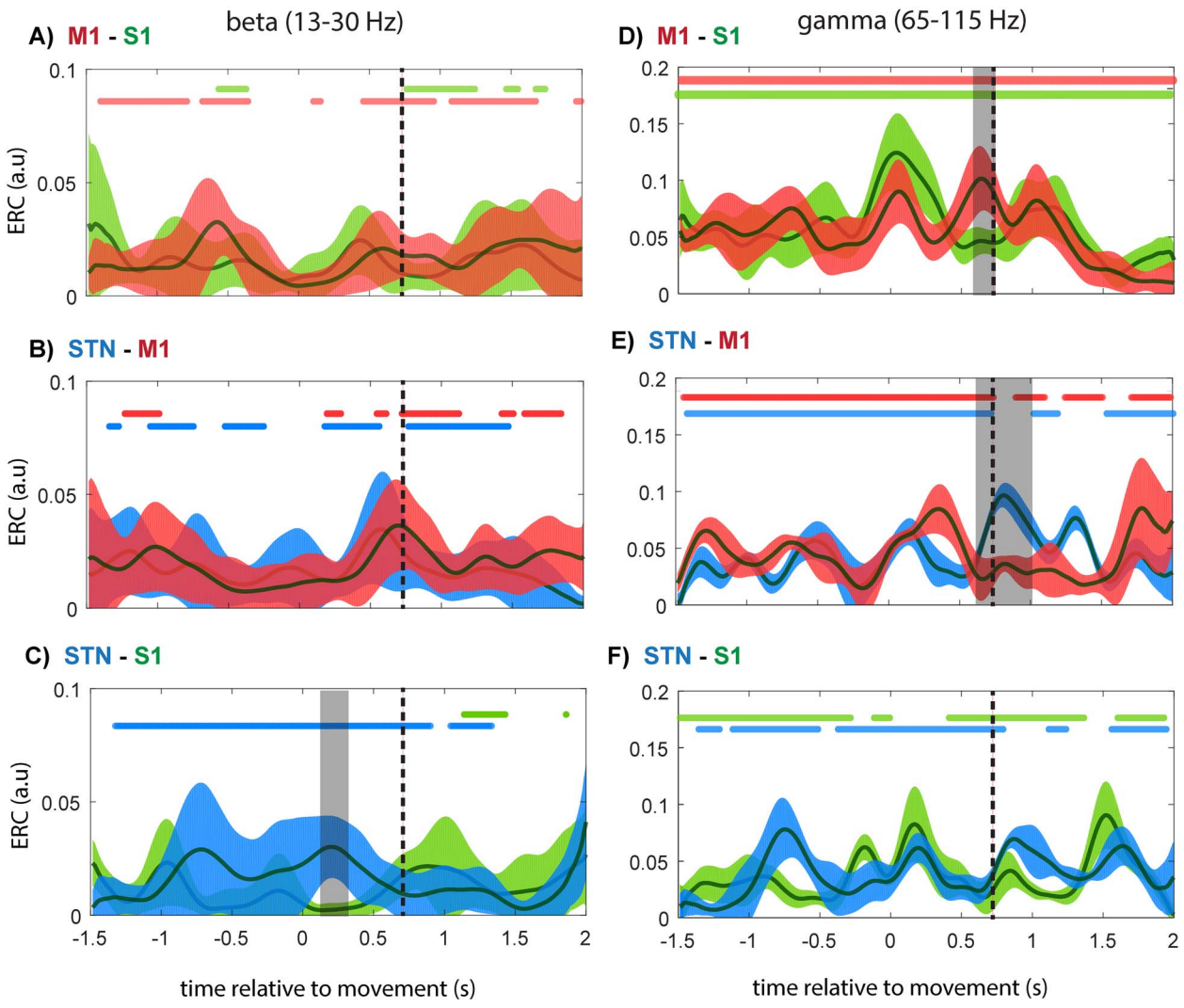

Figure 3. Event-related causality between M1, S1, and STN during movement execution. ERC values for (*A–C*) beta band and (*E* and *F*) gamma band between each location pair are plotted with colors representing the source of the causal interaction (e.g., in graph *A* (top-left), red plot represents propagation from M1 to S1 and green plot represents propagation from S1 to M1). Colored lines, at the top of each graph, represent time points of significant increase in group-average ERC, as compared with baseline (after FDR-correction). Gray shaded time points are those in which ERC is significantly different between the two flows. Mean ERC values are plotted as thin darker lines, with colored areas representing the confidence interval based on pooled-variance. Dotted line represents time of peak force generation.

synchronization of M1 input, in which cortical processing is overloaded, hampering information flow (Cole et al. 2017). Consistent with this model, we observed that when beta synchrony decreases prior to movement, gamma phase synchrony and the ability of STN gamma activity to predict M1/S1 gamma activity increases, prior to movement onset. Similarly, we previously reported that the pattern of STN spike to cortical phase-locking often is modulated before movement (Lipski et al. 2017).

The switch from the resting beta-dominant state to the pro-kinetic gamma-dominant state was marked by STN-M1 oscillatory phase alignment in the high-beta range, as well as a switch from bidirectional causal influence between M1 and STN beta activity to a predominantly unidirectional influence of STN beta on cortex, just prior to movement onset (see significance bars in Fig. 3B). The decrease in ability of M1 activity to predict STN activity may be an indication that the predominant beta influence on the STN at this point is not M1, but more likely premotor cortical regions, either via hyperdirect cortical afferents or through the striatal indirect pathway.

STN gamma phase-locking that was specific to M1 followed STN-M1 beta phase-locking preceded movement initiation. Across the entire cohort, gamma power increases preceded movement in M1 and S1, but occurred after movement onset in the STN, consistent with the idea that the basal ganglia modulate ongoing movements (Mazzoni et al. 2007), reviewed in (Turner and Desmurget 2010). Additionally, we discovered bidirectional information flow between the STN and both motor and sensory cortex during force transduction. Notably, M1 gamma activity strongly influenced STN gamma coincident with the generation of peak force. Subsequently, STN gamma phase-locking that was specific to S1 preceded the rebound of STN-M1 beta phase-locking and movement termination, suggesting that interactions between STN and S1 may be important for stopping an ongoing movement. Thus, our data demonstrate that narrow band gamma oscillations are

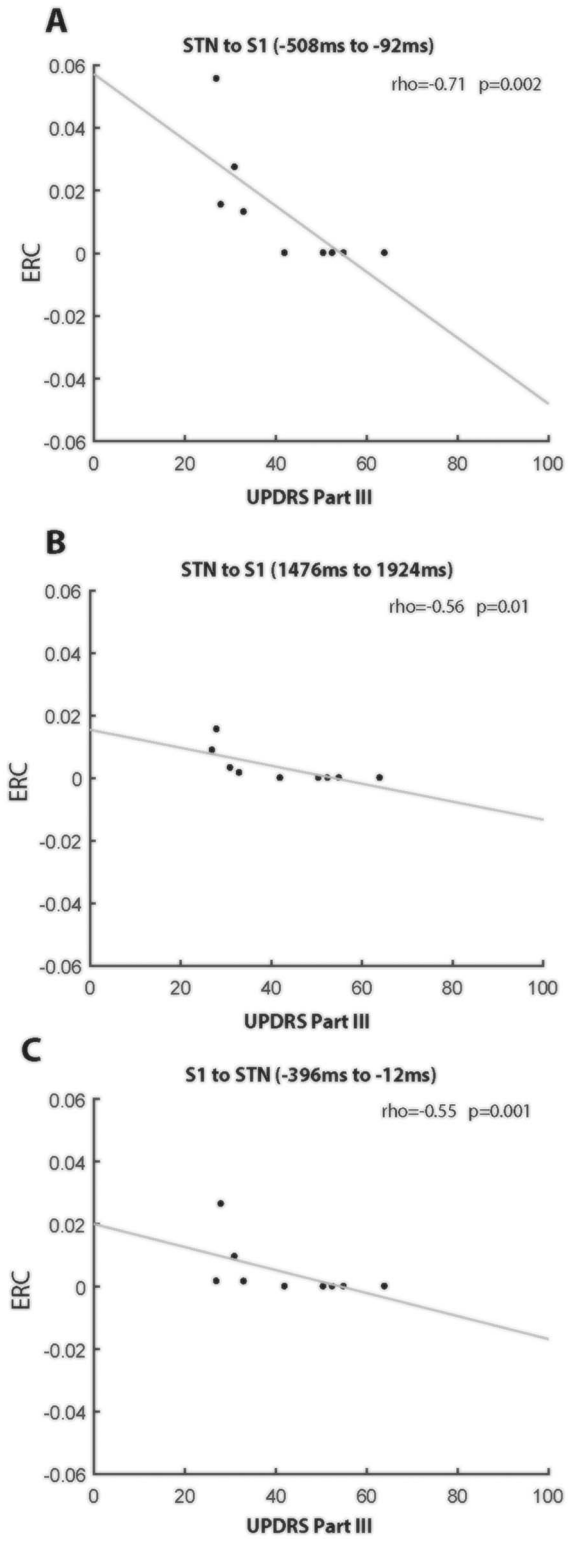

Figure 4. Event-related interactions with significant correlations to UPDRS score. A cluster-permutation test was used to define epochs of significant correlation between an interregional causal interaction and UPDRS scores. Scatter plots show the UPDRS scores for each subject and the mean ERC flow value between (*A* and *B*) STN to S1 and (*C*) S1 to STN during epochs where statistical significance was reached. The plotted line is the least square line fitted to the data. The average cluster Spearman rho value and *P*-value of the cluster are represented for each interaction.

used to coordinate not only primary motor and subcortical activity (Litvak et al. 2012) but also sensory cortical–subcortical interactions. Gamma interactions between M1, STN, and S1 appear to coordinate changes in the motor state, in line with previous data suggesting the role of gamma oscillations in facilitating cognitive processing in connected systems as seen in gamma phase synchrony facilitating processing across the visual cortex (Womelsdorf et al. 2006; Bosman et al. 2012) or memory encoding across hippocampal regions (Montgomery and Buzsaki 2007).

Somatosensory Integration

Traditional models of basal ganglia-cortical loop function do not address the role of primary sensory cortex in cortical-subcortical communication. The gating and conversion of sensory information into a form relevant for guiding movement, however, is one mechanism through which the basal ganglia may participate in motor control (Lidsky et al. 1985). Somatosensory cortex projects to the striatum in NHPs (Flaherty and Graybiel 1991, 1993, 1995), although only in rodents has the STN been reported to receive direct primary somatosensory inputs (Canteras et al. 1990). The high spatiotemporal resolution of ECoG allowed us to demonstrate the independent contributions of sensory cortex to motor control related to force transduction. Recent evidence that neuronal firing in the STN is entrained to S1 LFPs (Fischer et al. 2017; Lipski et al. 2017) further supports the presence of functional connectivity between the two regions.

Of all the spectral measures analyzed in this data set, only ERC measures related to sensory cortex were significantly correlated to PD motor symptom severity in the OFF-medication state. Motor symptom severity was associated with: 1) the magnitude of bidirectional interactions between STN and S1 beta activity during the motor planning period and 2) the magnitude of S1 influence on STN beta activity during movement termination. These results may provide a basis for ideas that PD involves abnormal sensory integration (Abbruzzese and Berardelli 2003), in that alterations in the sensory dynamics we describe may underlie the basis of some PD symptoms. We note that this idea also highlights a potential confound in this study, regarding our inability to differentiate normal from pathological sensory processing.

Summary

A novel combination of technical and computational methods was employed to provide the first evidence from humans that STN beta and gamma activity can predict similar activity in the cortex both prior to and during force transduction. In addition, we demonstrated that STN activity participates in somatosensory integration, and that interactions between the STN and somatosensory cortex predict PD symptom severity. These findings have important implications for understanding normal basal ganglia-cortical circuit neurophysiology and for understanding how circuit dysfunction can produce symptoms in movement disorders.

Supplementary Material

Supplementary data is available at *Cerebral Cortex* online.

Funding

National Institute of Neurological Disorders and Stroke (U01NS098969 to R.M.R., R01NS110424 to R.S.T. and R.M.R.); Walter Copeland Fund of the Pittsburgh Foundation (to R.M.R.). The authors declare no competing financial interests.

References

Abbruzzese G, Berardelli A. 2003. Sensorimotor integration in movement disorders. *Mov Disord*. 18:231–240.

Afsharpour S. 1985. Topographical projections of the cerebral cortex to the subthalamic nucleus. *J Comp Neurol*. 236:14–28.

Blinowska K, Kus R, Kaminski M, Janiszewska J. 2010. Transmission of brain activity during cognitive task. *Brain Topogr*. 23:205–213.

Bosman CA, Schoffelen JM, Brunet N, Oostenveld R, Bastos AM, Womelsdorf T, Rubehn B, Stieglitz T, De Weerd P, Fries P. 2012. Attentional stimulus selection through selective synchronization between monkey visual areas. *Neuron*. 75: 875–888.

Brainard DH. 1997. The psychophysics toolbox. *Spat Vis*. 10:433–436.

Brittain JS, Sharott A, Brown P. 2014. The highs and lows of beta activity in cortico-basal ganglia loops. *Eur J Neurosci*. 39:1951–1959.

Brown P, Oliviero A, Mazzone P, Insola A, Tonali P, Di Lazzaro V. 2001. Dopamine dependency of oscillations between subthalamic nucleus and pallidum in Parkinson's disease. *J Neurosci*. 21:1033–1038.

Canteras NS, Shammah-Lagnado SJ, Silva BA, Ricardo JA. 1990. Afferent connections of the subthalamic nucleus: a combined retrograde and anterograde horseradish peroxidase study in the rat. *Brain Res*. 513:43–59.

Cole SR, van der Meij R, Peterson EJ, de Hemptinne C, Starr PA, Voytek B. 2017. Nonsinusoidal Beta oscillations reflect cortical pathophysiology in Parkinson's disease. *J Neurosci*. 37:4830–4840.

Crone N. 1998a. Functional mapping of human sensorimotor cortex with electrocorticographic spectral analysis. II. Event-related synchronization in the gamma band. *Brain*. 121:2301–2315.

Crone N. 1998b. Functional mapping of human sensorimotor cortex with electrocorticographic spectral analysis. I. Alpha and beta event- related desynchronization. *Brain*. 121:2271–2299.

Crowell AL, Ryapolova-Webb ES, Ostrem JL, Galifianakis NB, Shimamoto S, Lim DA, Starr PA. 2012. Oscillations in sensorimotor cortex in movement disorders: an electrocorticography study. *Brain*. 135:615–630.

Dale AM, Fischl B, Sereno MI. 1999. Cortical surface-based analysis: I. Segmentation and surface reconstruction. *NeuroImage*. 9:179–194.

Deffains M, Bergman H. 2019. Parkinsonism-related β oscillations in the primate basal ganglia networks – recent advances and clinical implications. *Parkinsonism Relat Disord*. 59:2–8.

Delorme A, Makeig S. 2004. EEGLAB: an open source toolbox for analysis of single-trial EEG dynamics including independent component analysis. *J Neurosci Methods*. 134:9–21.

Desikan RS, Ségonne F, Fischl B, Quinn BT, Dickerson BC, Blacker D, Buckner RL, Dale AM, Maguire RP, Hyman BT *et al*. 2006. An automated labeling system for subdividing the human cerebral cortex on MRI scans into gyral based regions of interest. *NeuroImage*. 31:968–980.

Ding M, Bressler SL, Yang W, Liang H. 2000. Short-window spectral analysis of cortical event-related potentials by adaptive multivariate autoregressive modeling: data preprocessing, model validation, and variability assessment. *Biol Cybern*. 83:35–45.

Ewert S, Plettig P, Li N, Chakravarty MM, Collins DL, Herrington TM, Kühn AA, Horn A. 2018. Toward defining deep brain stimulation targets in MNI space: a subcortical atlas based on multimodal MRI, histology and structural connectivity. *NeuroImage*. 170:271–282

Fischer P, Lipski W, Neumann W-J, Turner RS, Fries P, Brown P, Richardson RM. 2018. Cortico-basal-ganglia communication: temporally structured activity for selective motor control. *bioRxiv*. 413286.

Fischer P, Pogosyan A, Herz DM, Cheeran B, Green AL, Fitzgerald J, Aziz TZ, Hyam J, Little S, Foltynie T *et al*. 2017. Subthalamic nucleus gamma activity increases not only during movement but also during movement inhibition. *elife*. 6. pii: e23947.

Flaherty AW, Graybiel AM. 1993. Two input systems for body representations in the primate striatal matrix: experimental evidence in the squirrel monkey. *J Neurosci*. 13:1120–1137.

Flaherty AW, Graybiel AM. 1991. Corticostriatal transformations in the primate somatosensory system. Projections from physiologically mapped body-part representations. *J Neurophysiol*. 66:1249–1263.

Flaherty AW, Graybiel AM. 1995. Motor and somatosensory corticostriatal projection magnifications in the squirrel monkey. *J Neurophysiol*. 74:2638–2648.

Flinker A, Korzeniewska A, Shestyuk AY, Franaszczuk PJ, Dronkers NF, Knight RT, Crone NE. 2015. Redefining the role of Broca's area in speech. *Proc Natl Acad Sci*. 112:2871–2875.

Fogelson N, Williams D, Tijssen M, Van Bruggen G, Speelman H, Brown P. 2006. Different functional loops between cerebral cortex and the subthalmic area in parkinson's disease. *Cereb Cortex*. 16:64–75.

Granger CWJ. 1969. Investigating causal relations by econometric models and cross-spectral methods. *Econometrica*. 37:424.

Groppe DM, Urbach TP, Kutas M. 2011. Mass univariate analysis of event-related brain potentials/fields I: a critical tutorial review. *Psychophysiology*. 48:1711–1725.

Haynes WIA, Haber SN. 2013. The organization of prefrontal-subthalamic inputs in primates provides an anatomical substrate for both functional specificity and integration: implications for basal ganglia models and deep brain stimulation. *J Neurosci*. 33:4804–4814.

Herz DM, Zavala BA, Bogacz R, Brown P. 2016. Neural correlates of decision thresholds in the human subthalamic nucleus. *Curr Biol*. 26:916–920.

Holm S. 1979. Board of the Foundation of the Scandinavian Journal of Statistics a simple sequentially rejective multiple test procedure a simple sequentially rejective multiple test procedure. *Scand J Stat*. 6:65–70.

Horn A, Li N, Dembek TA, Kappel A, Boulay C, Ewert S, Tietze A, Husch A, Perera T, Neumann WJ *et al*. 2019. Lead-DBS v2: towards a comprehensive pipeline for deep brain stimulation imaging. *NeuroImage*. 184:293–316.

Jenkinson N, Kühn AA, Brown P. 2013. Gamma oscillations in the human basal ganglia. *Exp Neurol*. 245:72–76.

Jensen O, Goel P, Kopell N, Pohja M, Hari R, Ermentrout B. 2005. On the human sensorimotor-cortex beta rhythm: sources and modeling. *NeuroImage*. 26:347–355.

Kondylis ED, Randazzo MJ, Alhourani A, Lipski WJ, Wozny TA, Pandya Y, Ghuman AS, Turner RS, Crammond DJ,

Richardson RM. 2016a. Movement-related dynamics of cortical oscillations in Parkinson's disease and essential tremor. *Brain*. 139:2211–2223.

Kondylis ED, Randazzo MJ, Alhourani A, Wozny TA, Lipski WJ, Crammond DJ, Richardson RM. 2016. High frequency activation data used to validate localization of cortical electrodes during surgery for deep brain stimulation. *Data Br*. 6:204–207.

Korzeniewska A, Crainiceanu CM, Kuś R, Franaszczuk PJ, Crone NE. 2008. Dynamics of event-related causality in brain electrical activity. *Hum Brain Mapp*. 29:1170–1192.

Korzeniewska A, Franaszczuk PJ, Crainiceanu CM, Kuł R, Crone NE. 2011. Dynamics of large-scale cortical interactions at high gamma frequencies during word production: event related causality (ERC) analysis of human electrocorticography (ECoG). *NeuroImage*. 56:2218–2237.

Lachaux JP, Rodriguez E, Martinerie J, Varela FJ. 1999. Measuring phase synchrony in brain signals. *Hum Brain Mapp*. 8:194–208.

Lalo E, Thobois S, Sharott A, Polo G, Mertens P, Pogosyan A, Brown P. 2008. Patterns of bidirectional communication between cortex and basal ganglia during movement in patients with Parkinson disease. *J Neurosci*. 28:3008–3016.

Lidsky TI, Manetto C, Schneider JS. 1985. A consideration of sensory factors involved in motor functions of the basal ganglia. *Brain Res Rev*. 9:133–146.

Lipski WJ, Wozny TA, Alhourani A, Kondylis E, Turner RS, Crammond DJ, Richardson RM. 2017. Dynamics of human subthalamic neuron phase-locking to motor and sensory cortical oscillations during movement. *J Neurophysiol*. 118:1472–1487 doi: 10.1152/jn.00964.2016.

Litvak V, Eusebio A, Jha A, Oostenveld R, Barnes G, Foltynie T, Limousin P, Zrinzo L, Hariz MI, Friston K *et al*. 2012. Movement-related changes in local and long-range synchronization in Parkinson's disease revealed by simultaneous magnetoencephalography and intracranial recordings. *J Neurosci*. 32:10541–10553.

Manning JR, Jacobs J, Fried I, Kahana MJ. 2009. Broadband shifts in local field potential power spectra are correlated with single-neuron spiking in humans. *J Neurosci*. 29:13613–13620.

Maris E, Oostenveld R. 2007. Nonparametric statistical testing of EEG- and MEG-data. *J Neurosci Methods*. 164:177–190.

Mazzoni P, Hristova A, Krakauer JW. 2007. Why Don't we move faster? Parkinson's disease, movement vigor, and implicit motivation. *J Neurosci*. 27:7105–7116.

Montgomery SM, Buzsaki G. 2007. Gamma oscillations dynamically couple hippocampal CA3 and CA1 regions during memory task performance. *Proc Natl Acad Sci*. 104:14495–14500.

Nambu A, Tokuno H, Inase M, Takada M. 1997. Corticosubthalamic input zones from forelimb representations of the dorsal and ventral divisions of the premotor cortex in the macaque monkey: comparison with the input zones from the primary motor cortex and the supplementary motor area. *Neurosci Lett*. 239:13–16.

Nishida M, Korzeniewska A, Crone NE, Toyoda G, Nakai Y, Ofen N, Brown EC, Asano E. 2017. Brain network dynamics in the human articulatory loop. *Clin Neurophysiol*. 128:1473–1487.

Panov F, Levin E, de Hemptinne C, Swann NC, Qasim S, Miocinovic S, Ostrem JL, Starr PA. 2017. Intraoperative electrocorticography for physiological research in movement disorders: principles and experience in 200 cases. *J Neurosurg*. 126:122–131.

Randazzo MJ, Kondylis ED, Alhourani A, Wozny TA, Lipski WJ, Crammond DJ, Richardson RM. 2016. Three-dimensional localization of cortical electrodes in deep brain stimulation surgery from intraoperative fluoroscopy. *NeuroImage*. 125:515–521.

Rosset A, Spadola L, Ratib O. 2004. OsiriX: an open-source software for navigating in multidimensional DICOM images. *J Digit Imaging*. 17:205–216.

Sherman MA, Lee S, Law R, Haegens S, Thorn CA, Hämäläinen MS, Moore CI, Jones SR. 2016. Neural mechanisms of transient neocortical beta rhythms: converging evidence from humans, computational modeling, monkeys, and mice. *Proc Natl Acad Sci*. 113:E4885–E4894.

Swann NC, De Hemptinne C, Miocinovic S, Qasim S, Wang SS, Ziman N, Ostrem JL, Luciano MS, Galifianakis NB, Starr PA. 2016. Gamma oscillations in the hyperkinetic state detected with chronic human brain recordings in parkinson's disease. *J Neurosci*. 36:6445–6458.

Tallon-Baudry C, Kreiter AG, Bertrand O. 1999. Sustained and transient oscillatory responses in the gamma and beta bands in a visual short-term memory task in humans. *Vis Neurosci*. 16:449–459.

Turner RS, Desmurget M. 2010. Basal ganglia contributions to motor control: a vigorous tutor. *Curr Opin Neurobiol*. 20:704–716.

Voytek B, Secundo L, Bidet-Caulet A, Scabini D, Stiver SI, Gean AD, Manley GT, Knight RT. 2010. Hemicraniectomy: a new model for human electrophysiology with high Spatio-temporal resolution. *J Cogn Neurosci*. 22: 2491–2502.

Williams D. 2002. Dopamine-dependent changes in the functional connectivity between basal ganglia and cerebral cortex in humans. *Brain*. 125:1558–1569.

Womelsdorf T, Fries P, Mitra PP, Desimone R. 2006. Gamma-band synchronization in visual cortex predicts speed of change detection. *Nature*. 439:733–736.

Yamawaki N, Stanford IM, Hall SD, Woodhall GL. 2008. Pharmacologically induced and stimulus evoked rhythmic neuronal oscillatory activity in the primary motor cortex in vitro. *Neuroscience*. 151:386–395.